IEEE Access
Multidisciplinary | Rapid Review | Open Access Journal

Received 28 October 2023, accepted 13 November 2023, date of publication 21 November 2023,
date of current version 30 November 2023.

Digital Object Identifier 10.1109/ACCESS.2023.3335390

RESEARCH ARTICLE

Research on Short-Circuit of Fault-Tolerant Permanent Magnet Rim Driven Motor Based on SPSRF-MPCC Algorithm

YONGHAN LIU, (Student Member, IEEE), JINGWEI ZHU, (Member, IEEE), JIUBO YUE, PING REN, (Student Member, IEEE), JIANG WU, AND XIANG LI
College of Marine Electrical Engineering, Dalian Maritime University, Dalian 116026, China

Corresponding author: Jingwei Zhu (zjwdl@dlmu.edu.cn)

This work was supported in part by the National Natural Science Foundation of China under Grant 52377037 and in part by the Stability Support Project of the Laboratory of Science and Technology on Integrated Logistics Support, National University of Defense Technology under Grant WDZC20235250309.

ABSTRACT The conventional double-vector model predictive current control algorithm based on rotating reference frame (RRF-MPCC) which used in fault-tolerant permanent magnet rim driven motor (FTPM-RDM) has the problems of large output torque ripple and long selection time of optimal voltage vector. Therefore, two novel MPCC algorithms based on six-phase stationary reference frame (SPSRF) without coordinate transformation are proposed in this paper to reduce torque ripple and computation burden. Both methods use the simplest computational steps to achieve the most effective control. The first method is the single-vector SPSRF-MPCC algorithm which groups alternative voltage vectors according to the magnitude of load torque. The second method is an improved double-vector combination optimal SPSRF-MPCC algorithm which makes two independent rounds of current prediction for each stator winding and goes through 61 space voltage vectors only 30 times compared with 122 times of conventional double-vector SPSRF-MPCC which also requires coordinate transformation. In addition, the fault-tolerant control of one-phase short-circuit is carried out with the current vector fault-tolerant control strategy. Finally, Through the comparison and verification of simulation and experiment, it is found that the double-vector SPSRF-MPCC algorithm can reduce the torque ripple and current fluctuation, and it can improve the stability and robustness of the system.

INDEX TERMS Fault-tolerant permanent magnet rim driven motor (FTPM-RDM), model predictive current control based on six-phase stationary reference frame (SPSRF-MPCC), current vector fault-tolerant (CVFT), short-circuit fault.

I. INTRODUCTION

To the national economy and people's life and property safety, the need of traffic and transportation is more and more urgent, especially the maritime transport industry. The demand for tonnage of ship grow rapidly. The traditional shafting propulsion system occupies a significant chunk of cabin space, which affects the utilization and propulsion efficiency [1], [2], [3]. In 1989, American scholar D. W was the first person to present the rim propeller [4]. After years of research and development, the rim propeller has been widely used in the field of ship propulsion for its high reliability, small vibration and low noise [5], [6]. The permanent magnet synchronous motor (PMSM) is widely used in the rim-driven propulsion system for its simple structure and high efficiency [7], [8]. However, the rim driven motor is prone to electrical failure cause it usually work under the water, and the PMSM mainly adopts the Y-type connection mode which has limited fault-tolerant capability [9]. The fault-tolerant permanent magnet rim driven motor (FTPM-RDM) has more than just the advantages of PMSM: It is of good fault-tolerant ability as well as stability with high efficiency due to the special structure design [10], [11].

The associate editor coordinating the review of this manuscript and approving it for publication was Jinquan Xu.

In order to bring the advantages of the FTPM-RDM into full play, it is necessary to study the control strategy. The model predictive control (MPC) algorithm is widely used in the field of motor control for its simple structure, fast dynamic response and suitable for nonlinear control systems [12]. For multi-phase PMSM, the common MPC is mainly divided into model predictive current control (MPCC) and model predictive torque control (MPTC) [13]. The MPCC algorithm possesses the features of smaller overshot, short adjusting time and higher precision, which is used widely in motor control system [14]. A novel method to determine the optimal voltage vector with only one calculation to reduce the calculation amount and current error proposed in [15]. The cost function containing current is converted to the cost function containing voltage, and the optimal non-zero vector is obtained by using the reference voltage obtained based on the principle of no beat, for which only the Angle information of the reference voltage need to determine. To reduce the complexity of the control system and current harmonics, [16] proposes an effective FCS-MPCC which combined with the construction of virtual vector space and duty cycle control without a modulator to drive PMSHM on the basis of [15]. For improving the steady state performance, two new multivector-operated MPCC methods which are applied to the surface-mounted PMSM to reduce torque and flux ripple are proposed in literature [17]. Both methods aim to determine the necessary changes in the stator-flux to reduce the stator current error during every sample. The algorithm is computationally efficient and does not need iterative prediction and cost function. But the switching frequency of the two methods is large. A two vector-based MPCC strategy, which extends the two vector combination to a combination between any two basic voltage vectors is proposed in [18]. However, this strategy requires ergodic optimization of 25 vector combinations, which brings great computational burden. In order to reduce the number of ergodic optimization, on the basis of conventional MPCC, literature [19] proposed two vector and three vector MPCC algorithms based on the different selection times of the voltage space vector in the optimization process, and adopted a cascade cost function optimization method to reduce the number of ergodicity to 14 times, reducing the calculation burden effectively. The conventional MPCC algorithm trend to follows the principle of free combination of voltage vectors, which leads to complicate in operation. To avoid this problem, [20] designed an optimized double-vector combination principle that can reduce the number of traversal optimization, and introduced the current tracking error term at the double-vector switch point in the cost function. This method ensures that the selected vector combination makes the current fluctuate less throughout the control period, but it requires several coordinate transformations and depends on parameter identification. In [17], three-vector MPCC was used to drive SPMSM, the first and second vectors were obtained by introducing virtual vectors combined with the cost function, and zero vectors were added to adjust the amplitude of the output voltage vector to reduce the current ripple, thus achieving the purpose of expanding the output modulation range. However, this method increases the computational burden due to the introduction of virtual vector.

MPCC algorithm is rarely applied to FTPM motor, especially to six-phase FTPM-RDM, which has the characteristics of multiple voltage vectors. Therefore, the application of MPC will face large computational problems. Reducing torque ripple and improving system robustness while achieving fault-tolerant operation will inevitably increase the complexity in system control. An enhanced virtual vector V3 MPCC fault-tolerant control strategy is used in [21] to solve the problem of reallocation of control schemes during open-circuit fault occurs, and the control methods before and after faults are unified. This method can effectively suppress the torque ripple after failure. Reference [22] uses normal vector space to decompose the transformation matrix without reconfiguration the controller topology for one-phase open-circuit fault occurred in asymmetric six-phase motor. By compensating 64 voltage vectors properly, 24 new virtual voltage vectors are synthesized to suppress current harmonics. This method does not require coordinate transformation, but the matrix decoupling process is complicated and calculation is large.

In view of the above, this paper takes the surface-mounted six-phase FTPM-RDM as control object and develops an improved double-vector MPCC algorithm based on six-phase stationary reference frame (SPSRF-MPCC). Firstly, this paper proposes a single-vector SPSRF-MPCC algorithm. Combined with the structure characteristics of FTPM-RDM, the voltage space vector is divided into groups according to the load torque to reduce calculation burden. Secondly, on the premise of minimizing torque ripple and current fluctuation, an improved double-vector combination optimal SPSRF-MPCC algorithm which goes through 61 space voltage vectors only 30 times without coordinate transformation is designed to reduce vector ergodic optimization times. In addition, a fault-tolerant control strategy based on current vector compensation is proposed. The fault phase current is compensated by the normal phase current vectors recombination directly under the condition of one-phase short-circuit fault. The method which is independent of the improved MPCC algorithm proposed in this paper not only does not need to change the control strategy after failure, but also able to suppress the torque ripple effectively. Finally, three MPCC methods are compared and simulated, and the effectiveness and superiority of the proposed algorithm are verified by experiments.

II. THE STRUCTURE AND MATHEMATICAL MODEL OF FTPM-RDM

The FTPM-RDM is a new type of electric propulsion device, which is different from the traditional motor structure. FTPM-RDM is designed by the combination of fault-tolerant

permanent magnet motor (FTPMM) and rim drive thruster (RDT) [23]. The propeller is combined with the rotor directly and it is driven by the rotation of the rotor, which can give full play to its advantages. This design is suitable for electric propulsion ships, which can improve their propulsion efficiency and space utilization. Its topology is shown in Fig. 1 and the H bridge inverter is shown in Fig. 2.

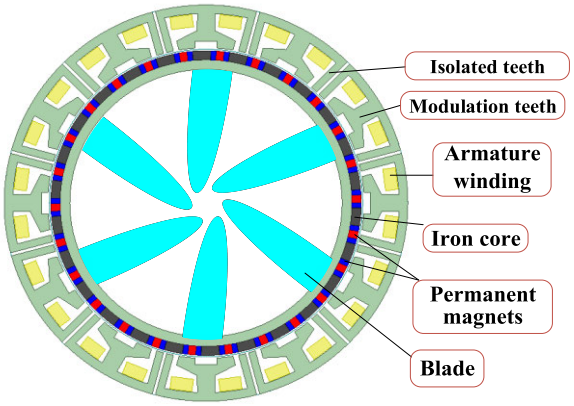

FIGURE 1. The topology diagram of FTPM-RDM.

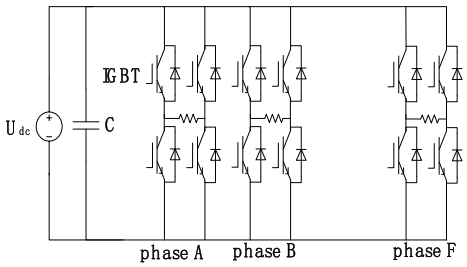

FIGURE 2. The H bridge inverter of FTPM-RDM.

The voltage equation of FTPM-RDM in SPSRF can be expressed as:

$$u_s = R_s i_s + \frac{\mathrm{d}}{\mathrm{d}t}\left[L_s i_s + \psi_f \cos\left(\omega_e t + \delta_s\right)\right] \tag{1}$$

where: u_s, i_s and δ_s are the voltages, currents and angle relative to phase A of each phase stator winding. "s" is represented by "A, B, C, D, E, F". R_s, ψ_f and L_s are for resistance, flux linkage, inductance respectively. ω_e is the electrical angular speed.

In order to solve the strong coupling characteristic of six-phase FTPM-RDM, it is necessary to decouple the original motor mathematical model to obtain the mathematical model under the two-phase RRF. The current equation in RRF can be expressed as:

$$\begin{aligned} u_d &= Ri_d + \frac{\mathrm{d}\psi_d}{\mathrm{d}t} - \omega_e \psi_q \\ u_q &= Ri_q + \frac{\mathrm{d}\psi_q}{\mathrm{d}t} + \omega_e \psi_d \end{aligned} \tag{2}$$

where $u_\mathrm{d}$and u_q are the voltages in dq RRF. i_d and i_q are the currents in dqRRF. ψ_d and ψ_d are the flux linkages in dq RRF, and their expressions are as follows:

$$\begin{cases} \psi_d = L_d i_d + \sqrt{\dfrac{3}{2}}\psi_f \\ \psi_q = L_q i_q \end{cases} \tag{3}$$

where L_d and L_q are the inductances in dq RRF. In the surface-mounted FTPM-RDM, $L_\mathrm{d} = L_q = L$. The electromagnetic torque equation can be expressed as:

$$T_e = n_p(\psi_d i_q - \psi_q i_d) \tag{4}$$

where n_p are the pole numbers.

III. CONVENTIONAL RRF-MPCC

The conventional MPCC algorithm uses the mathematical model of FTPM-RDM in dq RRF to implement control, i. e, deform equation (1):

$$\begin{aligned} \frac{\mathrm{d}i_\mathrm{d}}{\mathrm{d}t} &= \frac{u_\mathrm{d}}{L_\mathrm{s}} + \frac{-R_\mathrm{s} i_\mathrm{d} + \omega_\mathrm{e} L_\mathrm{s} i_\mathrm{q}}{L_\mathrm{s}} \\ \frac{\mathrm{d}i_\mathrm{q}}{\mathrm{d}t} &= \frac{u_\mathrm{q}}{L_\mathrm{s}} + \frac{-R_\mathrm{s} i_\mathrm{q} - \omega_\mathrm{e} L_\mathrm{s} i_\mathrm{d} - \omega_\mathrm{e}\psi_\mathrm{f}}{L_\mathrm{s}} \end{aligned} \tag{5}$$

In order to predict the future armature currents in dq RRF, the current prediction formula can be obtained by discretizing equation (6) in use of first-order forward Euler:

$$\begin{aligned} i_\mathrm{d}(k+1) &= (1 - \frac{R_\mathrm{s}T_\mathrm{s}}{L_\mathrm{s}})i_\mathrm{d}(k) + \frac{T_\mathrm{s}}{L_\mathrm{s}}u_\mathrm{d}(k) + \frac{T_\mathrm{s}}{L_\mathrm{s}}\omega_\mathrm{e}L_\mathrm{s}i_\mathrm{q}(k) \\ i_\mathrm{q}(k+1) &= (1 - \frac{R_\mathrm{s}T_\mathrm{s}}{L_\mathrm{s}})i_\mathrm{q}(k) + \frac{T_\mathrm{s}}{L_\mathrm{s}}u_\mathrm{q}(k) - \frac{T_\mathrm{s}}{L_\mathrm{s}}\omega_\mathrm{e}L_\mathrm{s}i_\mathrm{d}(k) \\ &\quad - \frac{T_\mathrm{s}}{L_\mathrm{s}}\omega_\mathrm{e}\psi_\mathrm{f} \end{aligned} \tag{6}$$

where $i_d(k)$ and $i_q(k)$ are the currents in dq axis at k period. $u_\mathrm{d}(k)$ and $u_\mathrm{q}(k)$ are the voltages in dq axis at k period.

Due to the large number of voltage vectors, the enumeration process of the 61 voltage vectors will take a certain time which can result in a time delay to the optimal switch action selection. That is, the voltage vector that should be active at the current time k will not be updated until the next time $(k+1)$. Therefore, the computation delay caused by digital signal processor (DSP) will increase the current harmonic and reduce the control performance. Hence, the compensation for this phenomenon is added to the control system to improve the control performance. Its principle is shown in Fig. 3. Where i_{ref} is the reference current.

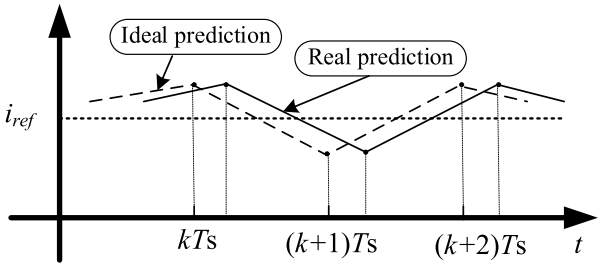

FIGURE 3. Schematic diagram of delay compensation.

The reference current in the adjacent control period is regarded as a fixed value. The current predicted model at $(k+2)$th cycle which is expressed in equation (7) after delay compensation can be obtained through the feedback current and voltage at $(k+1)$th cycle according to the current prediction equation (6), and it can be expressed as:

$$\begin{aligned} i_{\mathrm{d}}(k+2) &= (1-\frac{R_{\mathrm{s}}T_{\mathrm{s}}}{L_{\mathrm{s}}})i_{\mathrm{d}}(k+1)+\frac{T_{\mathrm{s}}}{L_{\mathrm{s}}}u_{\mathrm{d}}(k+1) \\ &\quad +\frac{T_{\mathrm{s}}}{L_{\mathrm{s}}}\omega_{\mathrm{e}}L_{\mathrm{s}}i_{\mathrm{q}}(k+1) \\ i_{\mathrm{q}}(k+2) &= (1-\frac{R_{\mathrm{s}}T_{\mathrm{s}}}{L_{\mathrm{s}}})i_{\mathrm{q}}(k+1)+\frac{T_{\mathrm{s}}}{L_{\mathrm{s}}}u_{\mathrm{q}}(k+1) \\ &\quad -\frac{T_{\mathrm{s}}}{L_{\mathrm{s}}}\omega_{\mathrm{e}}L_{\mathrm{s}}i_{\mathrm{d}}(k+1)-\frac{T_{\mathrm{s}}}{L_{\mathrm{s}}}\omega_{\mathrm{e}}\psi_{\mathrm{f}} \end{aligned} \tag{7}$$

In the conventional double-vector RRF-MPCC algorithm, the current prediction part is implemented as follows: The first voltage vector is selected from the candidate voltage vectors by using of a cost function based on the minimum value principle. Rational allocate the action time of the corresponding voltage vectors which is obtained by combining the first voltage vector with the other candidate voltage vector. Finally, the two voltage vectors are synthesized into a virtual voltage vector with adjustable direction and amplitude to realize the real-time control.

The cost function is an absolute value which includes the errors between the given current and the predicted current at $(k+2)$th time [24], as shown in formula (8).

$$g = |i_d^* - i_d(k+2)| + |i_q^* - i_q(k+2)| \tag{8}$$

where the superscript "$*$" represents the given currents of dq axis. Fig. 4 shows the block diagram of the conventional double-vector MPCC.

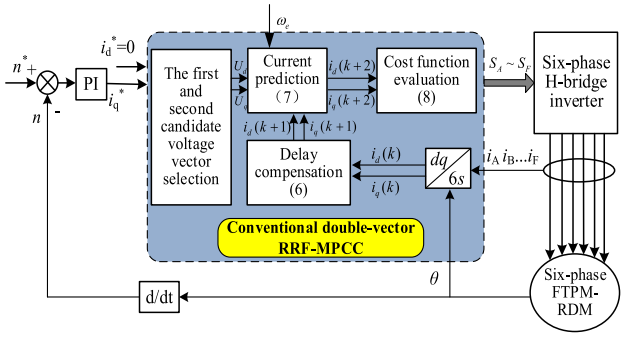

FIGURE 4. Block diagram of conventional double-vector MPCC.

The salient feature of the conventional double-vector RRF-MPCC is that it solves the problem of large steady-state ripple and poor steady-state performance in the case of there is a large deviation between the predicted and the given currents under single-vector RRF-MPCC control. However, the number of voltage vector is large. The two rounds of voltage vector selection need a total of 48 calculations, and each requires coordinate transformation even if the algorithm is simplified. Therefore, the conventional double-vector RRF-MPCC will inevitably impacts the control performance of FTPM-RDM.

IV. PROPOSED MPCC ALGORITHM BASED ON SPSRF

A. SINGLE-VECTOR MPCC BASED ON SPSRF

Since the conventional double-vector RRF-MPCC algorithm has a large computational quantity, a single-vector MPCC algorithm based on SPSRF is proposed in this paper to reduce the computational burden.

The strong isolation characteristic of six-phase FTPMM can get the mutual inductance of each phase winding approximately to zero. From this, the equation (1) can be deformed as:

$$\frac{\mathrm{d}}{\mathrm{d}t}i_s = \frac{1}{L_s}\left(u_s - R_s i_s + \omega_e \psi_f \sin(\theta - \delta_s)\right) \tag{9}$$

where: θ is the rotor position. In order to predict the future armature currents in SPSRF, the current prediction formula can be obtained by discretizing equation (9) in use of first-order forward Euler:

$$\begin{aligned} i_s(k+1) &= (1-\frac{R_s T_s}{L_s})i_s(k) \\ &\quad +\frac{T_s}{L_s}\left(u_s(k)+\omega_e\psi_f\sin(\theta-\delta_s)\right) \end{aligned} \tag{10}$$

where $i_s(k)$ is the current in SPSRF at k period. $u_s(k)$ is the voltage in SPSRF at k period.

Similarly, from Fig. 3, the current predicted model at $(k+2)$th cycle after delay compensation can be calculated by the predicted $(k+1)$th values, and it can be expressed as:

$$\begin{aligned} i_s(k+2) &= (1-\frac{R_s T_s}{L_s})i_s(k+1) \\ &\quad +\frac{T_s}{L_s}\left(u_s(k+1)+\omega_e\psi_f\sin(\theta-\delta_s)\right) \end{aligned} \tag{11}$$

where $i_s(k+1)$ and $u_s(k+1)$ are the currents and voltages in SPSRF at $(k+1)$ period.

From a detailed analysis of the six-phase H-bridge inverter circuit, it is clear that it has 729 switching states and 343 space voltage vectors synthesis without cancellation. Each synthetic vector has multiple switch combinations and taking voltage vector amplitude 4 as an example, it is synthesized as shown in Fig. 5 (b). By removing duplicated vectors 61 space voltage vectors with different amplitude and phase which shown in Fig. 5 (a) can be obtained.

In order to enhance efficiency in utilization of voltage space vector and take into account the performance of MPCC algorithm, alternative voltage vector groups with different amplitude are selected according to the load torque during the control process. With 50% of the rated torque as the distinguishing point and fully considering the symmetry of the voltage vector combination, the alternative voltage vector combination is limited to the following two cases.

(1) The load torque is less than 50% of the rated torque and the amplitude of the alternative voltage vector is 2.

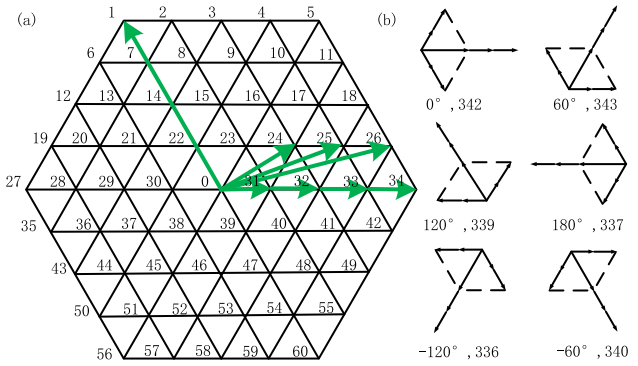

FIGURE 5. Schematic diagram of delay compensation.

The corresponding voltage vector is shown in Fig. 6. Taking U_{32} vector as an example, the switch state is defined phase A and phase U as effective phases. The other phases should balance each other.

(2) The load torque is more than 50% of the rated torque and the amplitude of the alternative voltage vector is 4. The corresponding voltage vector is shown in Fig. 6. Taking U_{34} vector as an example, the switch state is defined all phases as effective phases.

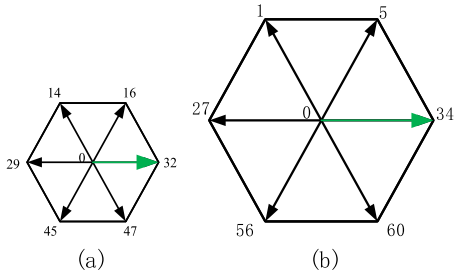

FIGURE 6. Voltage space vector diagram with amplitude 2 (a) and 4 (b).

The alternative voltage vector combinations are shown in Table 1.

TABLE 1. Alternative vector combinations.

$T_e \le 0.5T_n$		$T_e > 0.5T_n$	
Voltage vector	Switch status	Voltage vector	Switch status
u_{32}	(1,1,-1,-1,1,-1)	u_{34}	(1,1,-1,-1,-1,1)
u_{16}	(-1,1,1,-1,-1,1)	u_5	(1,1,1,-1,-1,-1)
u_{14}	(1,-1,1,1,-1,-1)	u_1	(1,1,1,1,-1,-1)
u_{29}	(1,1,-1,1,1,-1)	u_{27}	(-1,-1,1,1,1,-1)
u_{45}	(-1,1,-1,-1,1,1)	u_{56}	(-1,-1,-1,1,1,1)
u_{47}	(1,-1,-1,1,-1,1)	u_{60}	(1,-1,-1,-1,1,1)

After identifying the candidate voltage vectors table, the corresponding predicted six-phase currents can be obtained by substituting the candidate voltage vectors into $u_s(k+1)$ of the equation (11). The control voltage vectors are evaluated by the following cost function (12).

$$g = \sum |i_s^* - i_s(k+2)| \tag{12}$$

where i_s^* represents the six-phase reference currents.

The block diagram of this control scheme is shown in Fig. 7. This control scheme has omitted the step of coordinate transformation in conventional double-vector MPCC. The current prediction is carried out in the SPSRF directly. It reduces the computational burden, to a certain extent. However, the utility ratio of the voltage vector is low with only one vector is selected in each circle. Therefore, the voltage vectors of this control scheme still requires further utilization.

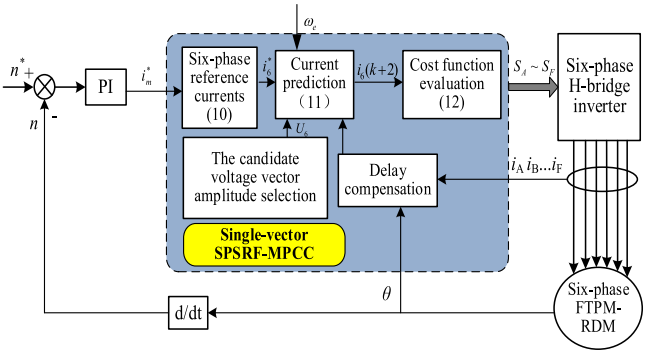

FIGURE 7. The control structure diagram of the double-vector MPCC algorithm.

B. IMPROVED DOUBLE-VECTOR MPCC ALGORITHM BASED ON SPSRF

The voltage vector number of FTPM-RDM is big with a total of 61. It indicates that the candidate voltage vector combination for implementing double-vector RRF-MPCC would be highly impracticable due to the large computation burden and complexity. The single-vector SPSRF-MPCC can reduce the calculation burden in the prediction process, but the utilization of the space voltage vector is not high in view of only one vector is selected in each cycle. In order to improve utilization of the candidate voltage vectors, a double-vector MPCC algorithm based on SPSRF is proposed, which predict the stator current of each phase separately.

This algorithm makes two independent rounds of current prediction for each phase and different candidate voltage vectors are selected in the two rounds. In the first round, the nonzero voltage vector −1 and 1 are selected as the alternative H-bridge switch states and it can be expressed as:

$$\begin{bmatrix} u_{sm1} \\ u_{sm2} \end{bmatrix} = \begin{bmatrix} 1 \\ -1 \end{bmatrix} \cdot U_{dc} \tag{13}$$

where U_{dc} is the DC voltage. Only a total of 12 calculations are required to cover 61 voltage vectors. In the second round, the voltage vector -1, 0 and 1 are selected as the alternative H-bridge switch states and it can be expressed as:

$$\begin{bmatrix} u_{sn1} \\ u_{sn2} \\ u_{sn3} \end{bmatrix} = \begin{bmatrix} 1 \\ 0 \\ -1 \end{bmatrix} \cdot U_{dc} \tag{14}$$

Two rounds of current prediction need to be accomplished as to achieve the MPCC algorithm, and the second round requires 18 calculations. Take phase A as an example, the predicted current in the first round are obtained after discretization and delay compensation can be expressed as:

$$\begin{aligned} i_A(k+2) = (1 - \frac{R_s T_s}{L_s}) i_A(k+1) \\ + \frac{T_s}{L_s} u_A(k+1) + \omega_e \psi_f \sin\theta_A \end{aligned} \tag{15}$$

Two sets of predicted currents $i_{Am1}(k+2)$ and $i_{Am2}(k+2)$ can be obtained by substituting the candidate voltage vectors u_{Am1} and u_{Am2} in equation (13) into (15). The optimal voltage vector is selected by the cost function (16), which is applied to phase A as the first voltage vector.

$$g = |i_s^* - i_s(k+2)| \tag{16}$$

The second round current prediction predict the current based on the principle of deadbeat control. The prediction formula is:

$$i_A(k+2) = i_A(k+1) + S_{Am} t_{Am} + S_{An} t_{An} = i_A^* \tag{17}$$

where S_{Am} and S_{An} are the current slope under the action of two round voltage vectors. t_{Am} and t_{An} are the action time of u_{Am} and u_{An} respectively. u_{An} is the voltage vector determined after the second round prediction.

S_{Am} can be calculated by equation (18) and S_{An} can be obtained by plugging the three candidate voltage vectors of the second round into equation (14). The calculation formula are expressed as:

$$\begin{aligned} S_0 &= \frac{1}{L_s}(-R_s i_A + \omega_e \psi_f \sin\theta_A) \\ S_{Amn} &= S_0 + \frac{u_{Amn}}{L_s} \end{aligned} \tag{18}$$

By combining the three candidate voltage vectors of the second round with the voltage vectors determined in the first round, the voltage vector combination which is obtained in phase A are shown in Table 2.

TABLE 2. The second round predicts voltage vector combination.

Combination	u_{Am}	u_{An}
1	u_{Am1}	u_{An1}
2	u_{Am1}	u_{An2}
3	u_{Am1}	u_{An3}

The action time of the two sets of voltage vectors can be obtained from equation (19) and it can be expressed as:

$$\begin{aligned} t_{Am} &= \frac{i_A^* - i_A(k+1) - S_{An} T_s}{S_{Am} - S_{An}} \\ t_{An} &= T_s - t_{Am} \end{aligned} \tag{19}$$

The synthesized voltage vector in SPSRF can be expressed as:

$$u_A = \frac{t_{Am}}{T_s} u_{Am} + \frac{t_{An}}{T_s} u_{An} \tag{20}$$

The six-phase current prediction process is carried out simultaneously without interference. The above calculation method is also applicable for other five phases.

V. SHORT-CIRCUIT FAULT-TOLERANT CONTROL STRATEGY

Of all motor faults, short-circuit fault is a frequent failure. In [25], an open-circuit fault is studied by using flux compensation strategy. The flux linkage is bound to change when one open-circuit fault occurs. In this reference, the fault phase is compensated by the remaining five normal phase flux linkages, and the compensated stator flux linkage is expressed as follows. Take phase A as an example.

$$\begin{aligned} \psi_A^* = |\psi_s|^* \cos\left(\theta_s + \Delta\sigma(k+1) - \frac{h-1}{3}\pi\right) \\ - \psi_f \cos\left(\theta - \frac{h-1}{3}\pi\right) \end{aligned} \tag{21}$$

Although this method can achieve fault compensation, it is difficult to guarantee the conservation of torque. According to the output torque of FTPM-RDM in normal operation:

$$T_e = \frac{1}{\omega_m}(e_A i_A + e_B i_B + e_C i_C + e_D i_D + e_E i_E + e_F i_F) \tag{22}$$

where $e_A \sim e_F$ are the Back-EMF of each phase. ω_m is the mechanical angular velocity. When phase A has an short-circuit, $e_A i_A$ is equal to zero, and the output torque is no longer conserved. From [26], the current of the remaining five normal phases is used to compensate phase A in $\alpha\beta$ SRF, which can ensure that the vector composition effect is unchanged and the output torque is conserved. In this paper, it is improved and applied to short-circuit fault. The specific compensation method is as follows:

$$\begin{cases} i_B^* = i_B + i_A/3 - i_{SA}/3 \\ i_C^* = i_C - i_A/3 + i_{SA}/3 \\ i_D^* = i_D - i_A/3 + i_{SA}/3 \\ i_E^* = i_E - i_A/3 + i_{SA}/3 \\ i_F^* = i_F + i_A/3 - i_{SA}/3 \end{cases} \tag{23}$$

By substituting the compensated reference current (19) into the equation (22), it can be obtained that $T_e^* = T_e$.

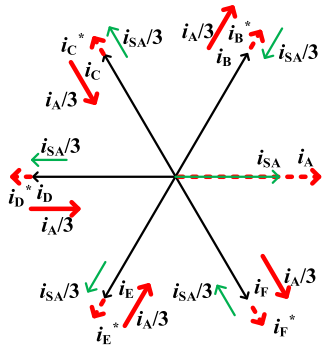

FIGURE 8. Current vector diagram after single-phase short-circuit fault condition.

That is, the torque ripple can be reduced and the torque conservation can be realized by using current vector fault-tolerant (CVFT) when phase A short-circuit fault occurs. The control structure diagram of the double-vector SPSRF-MPCC algorithm is shown in Fig. 9.

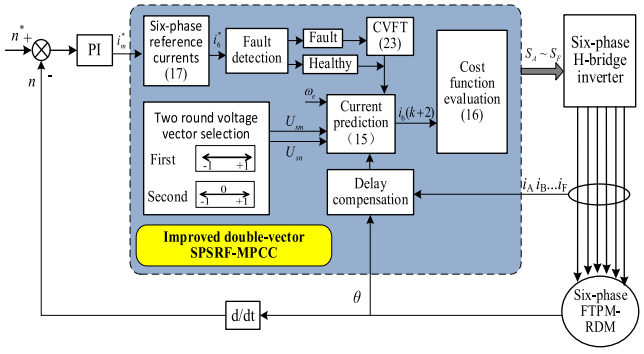

FIGURE 9. The control structure diagram of the double-vector SPSRF-MPCC algorithm.

The six-phase current prediction process is carried out simultaneously without interference. The flow chart of phase A current prediction process based on double-vector SPSRF-MPCC algorithm is shown in Fig. 10.

VI. SIMULATION VERIFICATION

Establishing a simulink model in use of Matlab/Simulink to verify the feasibility of the improved algorithm. The parameters of the six-phase FTPM-RDM in the simulation are shown in Table 3. the sampling frequency of the simulation model is set as 10 kHz to make sure of the simulation effect satisfies the request of actual application.

Torque ripple is an important evaluation condition for evaluating the quality of motor control algorithms. For comparison, the torque ripple equation is defined as follows:

$$T_{ripple} = \frac{\max\left\{\left|T_{max} - T_{avg}\right|, \left|T_{avg} - T_{min}\right|\right\}}{T_{avg}} \quad (24)$$

where T_{max}, T_{avg} and T_{min} are the maximum, average and minimum values of torque.

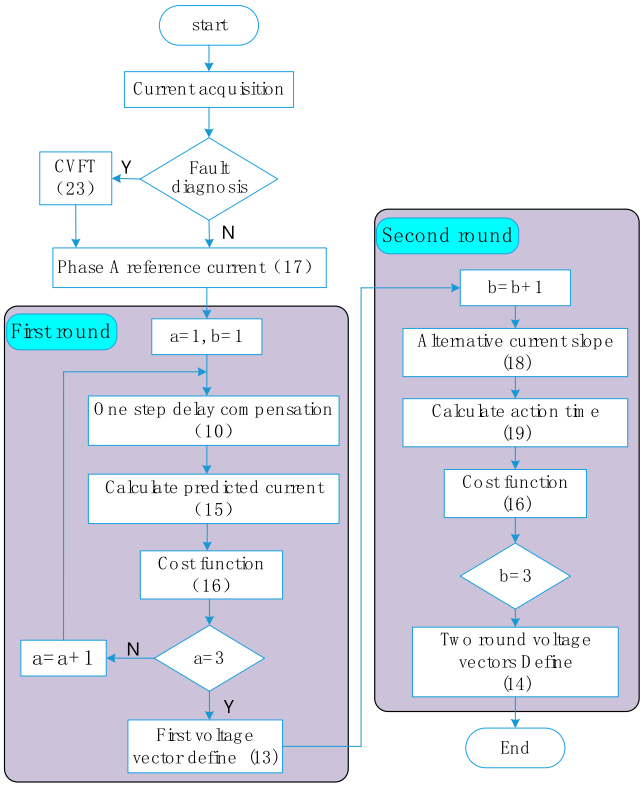

FIGURE 10. Flow chart of the proposed double-vector SPSRF-MPCC algorithm.

TABLE 3. FTPM-RDM simulation experiment parameters.

Parameters	Variable symbol and unit	Value
Stator resistance	R, Ω	1.2
Rated speed	N, (r/min)	600
Winding inductance	L, mH	27.42
Rated power	P, KW	1.5

A. STEADY-STATE SIMULATION

Fig. 11 shows the simulation results of the double-vector RRF-MPCC and single-vector SPSRF-MPCC compared with the improved double-vector SPSRF-MPCC. The FTPM-RDM operates stably at 500r/min with 15Nm load. The phase current harmonic distortion and torque ripple of the double-vector RRF-MPCC are 11.07% and 18.78%, the phase current harmonic distortion and torque ripple of the single-vector SPSRF-MPCC are 7.72% and 11.98%. while the improved double-vector SPSRF-MPCC are 4.22% and 4.67%.The result shows that the current control accuracy of the improved double-vector SPSRF-MPCC is better than that of the double-vector RRF-MPCC and the single-vector SPSRF-MPCC, and the improvement of torque ripple is much more obvious than that of the double-vector RRF-MPCC. The improved algorithm has a good static performance and the simulation results of the three algorithms are detailed in Table 4.

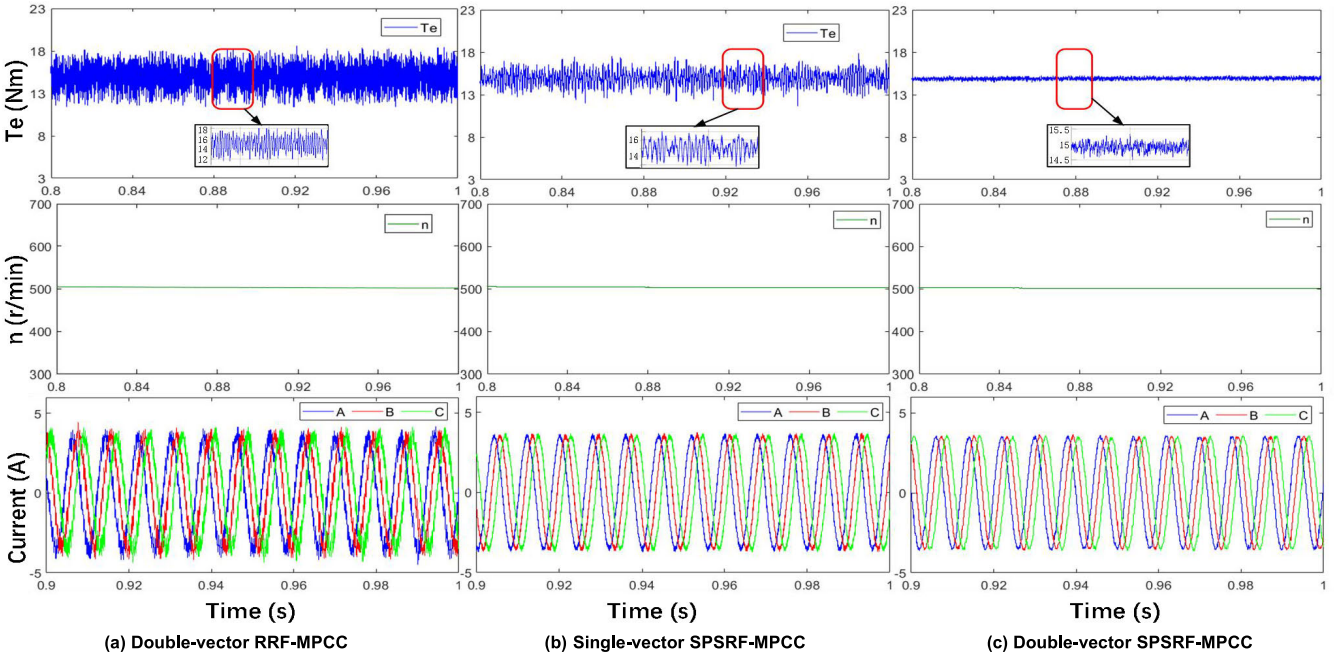

FIGURE 11. Steady state simulation results of FTPM-RDM using three MPCC algorithms.

TABLE 4. Comparison between three MPCC algorithms.

Term	Double-vector RRF-MPCC	Single-vector SPSRF-MPCC	Double-vector SPSRF-MPCC
Harmonic distortion	11.07%	7.72%	4.22%
Torque ripple	18.78%	11.98%	4.67%

B. DYNAMIC SIMULATION

1) SIMULATION RESULTS UNDER HEALTHY CONDITION

In the control performance simulation, besides the steady state experiment, the proposed algorithm is also verified by simulation for the sake of dynamic responses performance, which is divided into two types: speed step and torque step.

Fig. 12 shows the dynamic characteristics of the FTPM-RDM with 15Nm load running at speed change condition. The initial speed is 200r/min and it abrupt change of 500r/min at 1.2s. From the speed diagram of Fig 12, the FTPM-RDM can run smoothly according to the specified speed under the three algorithms, and the jitter is small under the low speed. The torque ripple of the FTPM-RDM under different speeds during stable operation is shown on the upper half of the image. The torque ripple is obvious in Double-vector RRF-MPCC. Combined with the local up-scaling diagram of torque at 200r/min, it can be found through comparison that the torque ripple is small under the improved double-vector SPSRF-MPCC, and the torque stability is increased by 8.12% compared with the single-vector SPSRF-MPCC. The torque stability effect of the improved method is significantly improved.

Figure 13 shows the dynamic characteristics of the FTPM-RDM with the speed of 200r/min at load change condition. The motor starts with a 10Nm load and switches to 15Nm at 1.2s. As can be seen from the speed diagram, the speed fluctuation is about 7r/min under the improved double-vector SPSRF-MPCC as the torque changes, it is smaller than that of the single-vector SPSRF-MPCC and much smaller than double-vector RRF-MPCC. In the three cases, the steady operation can all be ensured and in, the speed recovery time of the double-vector SPSRF-MPCC is smallest about 0.39s. The torque ripple under the improved double-vector SPSRF-MPCC algorithm is nearly the same, with 3.91% and 4.36% respectively before and after the load change. It is significantly improved compared with the other two MPCC algorithms.

It can be concluded that the combination of analysis covering different simulation condition makes the improved double-vector SPSRF-MPCC algorithm more suits to the dynamic changes of FTPM-RDM.

2) SIMULATION RESULTS UNDER ONE PHASE SHORT-CIRCUIT CONDITION

Fig. 14 shows the torque and current simulation results by using of the improved double-vector SPSRF-MPCC algorithm under one-phase short-circuit condition. CVFT strategy is used for compensating the short-circuit fault

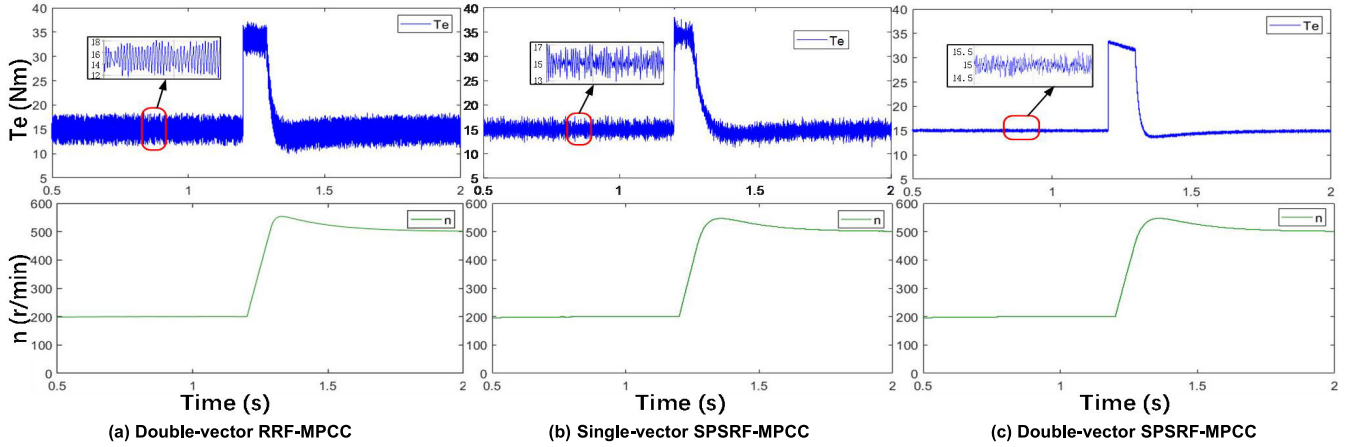

FIGURE 12. Simulation results of FTPM-RDM using two MPCC algorithms under the speed change.

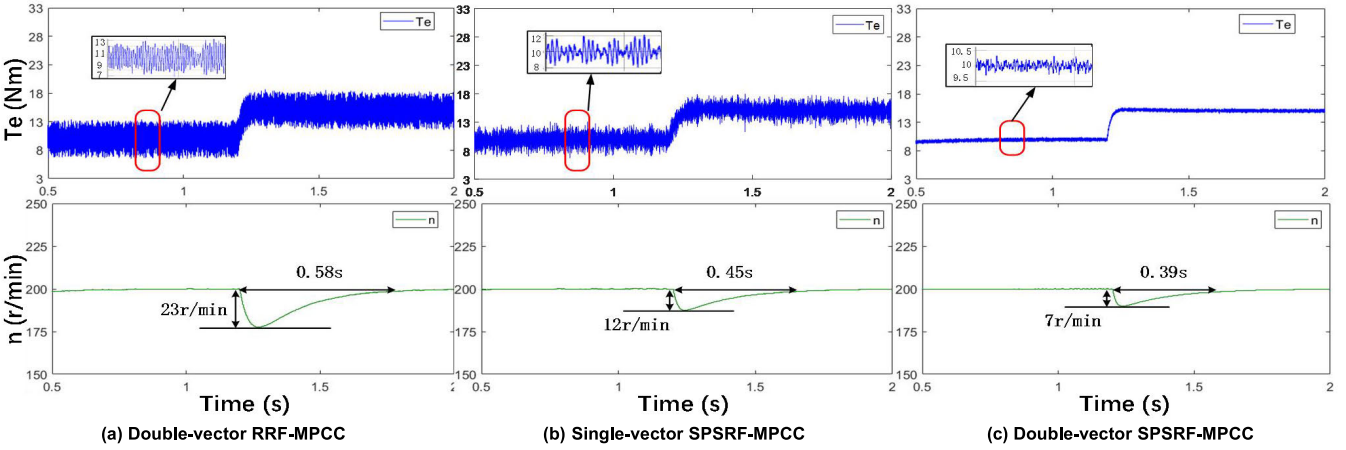

FIGURE 13. Simulation results of FTPM-RDM using two MPCC algorithms under the load change.

of FTPM-RDM. The given speed of the motor is 500r/min and it works under 15Nm load. A short-circuit fault occurs in phase A at 1.2s and the fault tolerant control strategy is added at 1.4s.

When a short-circuit fault occurs in phase A, the phase of the phase A current is opposite to the given current phase, generating the torque which can prevents the motor normal operation. From Fig. 14, the short-circuit fault has a significant impact on the motor torque, and its torque ripple reaches 24.23%. When the CVFT control strategy is added at 1.4s, the torque ripple is about 6.21%, which is significantly reduced, although it is higher than the 3.65% before the fault, it ensures the normal and stable operation and is within an acceptable range.

Combined with the current waveform in Fig. 14 and enlarge the current diagram within 0.02s of each stage locally. The current amplitude of phase B after fault-tolerance increases the most, which accords with the derivation results of fault-tolerant control theory in equation (19). The simulation indicates that the fault-tolerant strategy is effective and can ensure the stable operation under one phase short-circuit condition.

VII. EXPERIMENT VERIFICATION

In this paper, the validity of the proposed control strategy is verified by the six-phase FTPM-RDM vector control system hardware experiment platform as shown in Fig. 15. This platform mainly includes six-phase FTPM-RDM, motor controller, hardware circuit and upper computer. Fast control prototype Rapid Control Prototyping (RCP) is selected as the core controller of motor control. It can download the control algorithm written by simulink into the real-time fast control prototype hardware to realize fast and accurate control. The motor parameters used in the experiment are the same as used in MATLAB. The hardware sampling frequency is 10 kHz.

The experiment of the proposed MPCC algorithms are specifically divided into steady state operation and dynamic

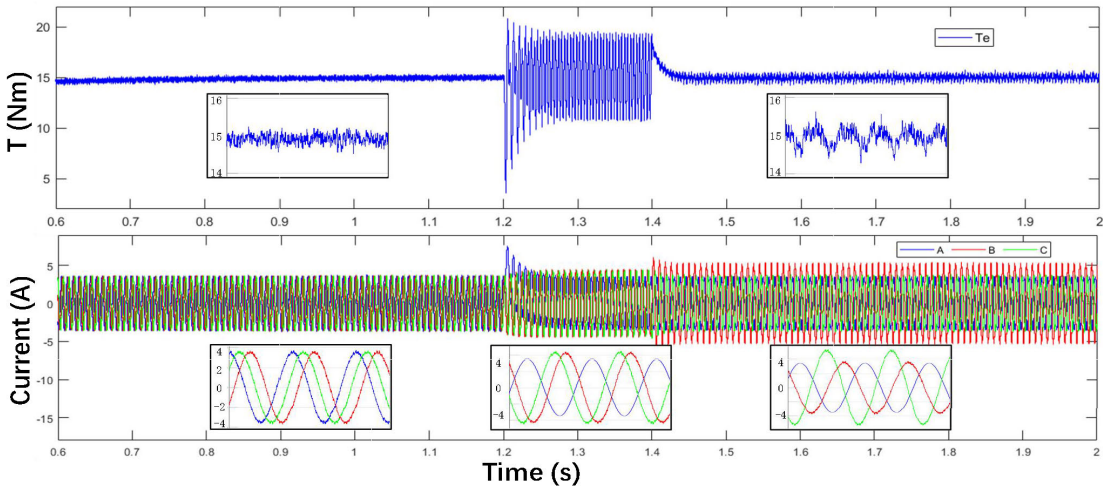

FIGURE 14. Simulation results of FTPM-RDM using double-vector SPSRF-MPCC before and after phase A short-circuit fault.

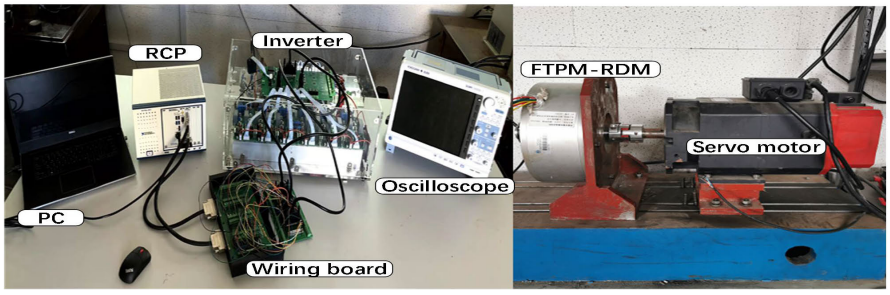

FIGURE 15. FTPM-RDM hardware experimental platform.

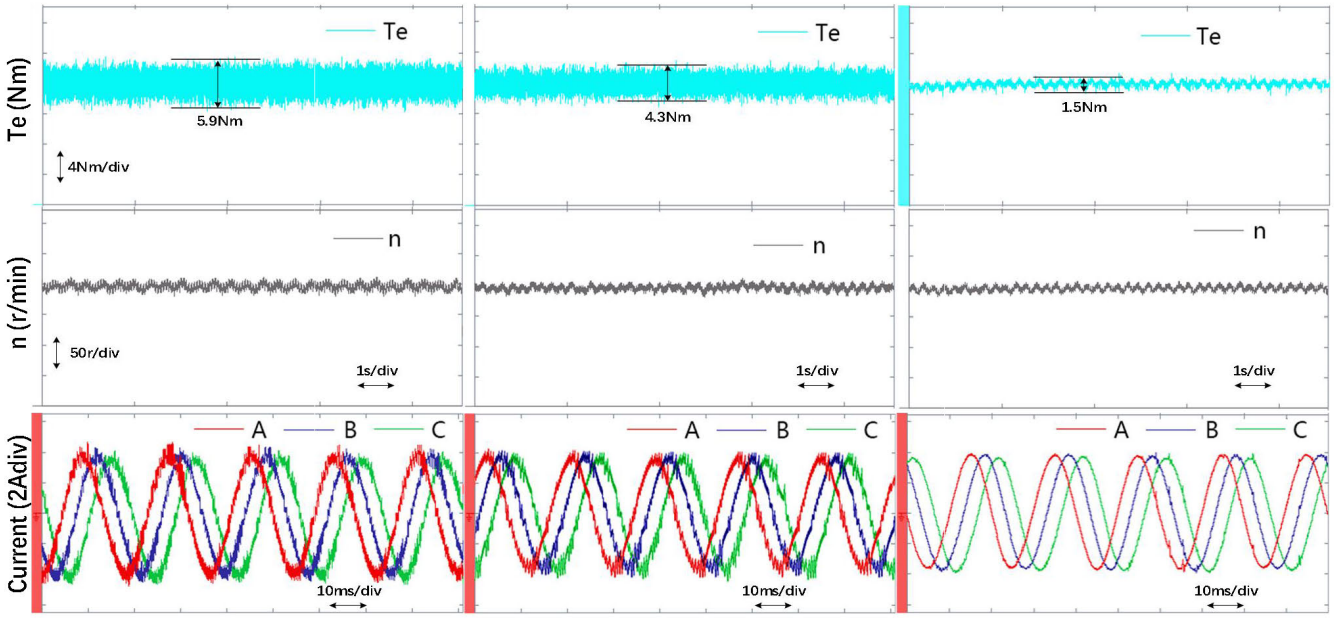

(a) Double-vector RRF-MPCC (b) Single-vector SPSRF-MPCC (c) Double-vector SPSRF-MPCC

FIGURE 16. Experiment results of FTPM-RDM using two MPCC algorithms under the load change.

operation with variable load and speed. Furthermore an short-circuit fault of phase A is simulated during the dynamic operation, in which the change of the torque and current are observed by adding fault-tolerant strategy.

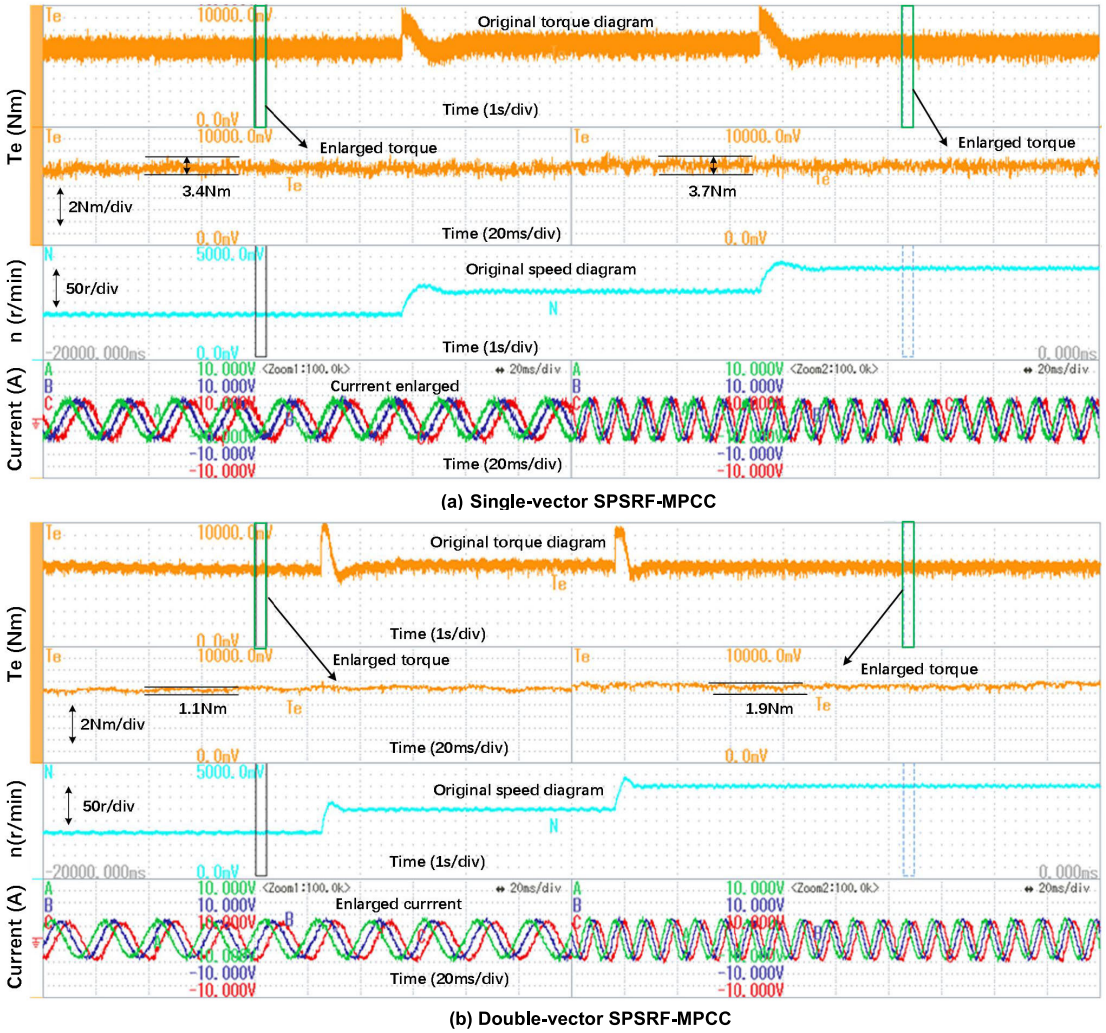

FIGURE 17. Dynamic experimental results of FTPM-RDM using two SPSRF-MPCC algorithms.

A. VERIFICATION EXPERIMENT OF STEADY-STATE OPERATION RESULTS

The FTPM-RDM runs stably at 200r/min with 16Nm load. The comparison waveform results of the three experiments are shown in Fig. 16. From the diagram, the torque ripple of the double-vector RRF-MPCC is 17.28%, the single-vector SPSRF-MPCC is 12.14%, while the improved double-vector SPSRF-MPCC is 6.18%. The speed fluctuation in double-vector SPSRF-MPCC is small, and its sine property of the current is obviously better than that of the other two MPCC algorithms. The experimental results show that better control performance can be obtained by using of the double-vector SPSRF-MPCC. The experiment results of the three MPCC algorithms are summarized in Table 5 for better presentation.

The computations required for double-vector SPSRF-MPCC is only 30 times which is much less than that of the double-vector RRF-MPCC required 122 times. To better reflect the advantages of the improved algorithm in terms of calculation amount, the calculation time of the three algorithms are shown in Table 6. The computation time required by the two proposed algorithms which reduce

TABLE 5. Comparison between three MPCC algorithms.

Term	Double-vector RRF-MPCC	Single-vector SPSRF-MPCC	Double-vector SPSRF-MPCC
Torque ripple	17.28%	12.14%	6.18%

TABLE 6. Implementation details of the three MPCC algorithms.

Term	Double-vector RRF-MPCC	Single-vector SPSRF-MPCC	Double-vector SPSRF-MPCC
calculation time (μs)	47.52	23.27	22.31

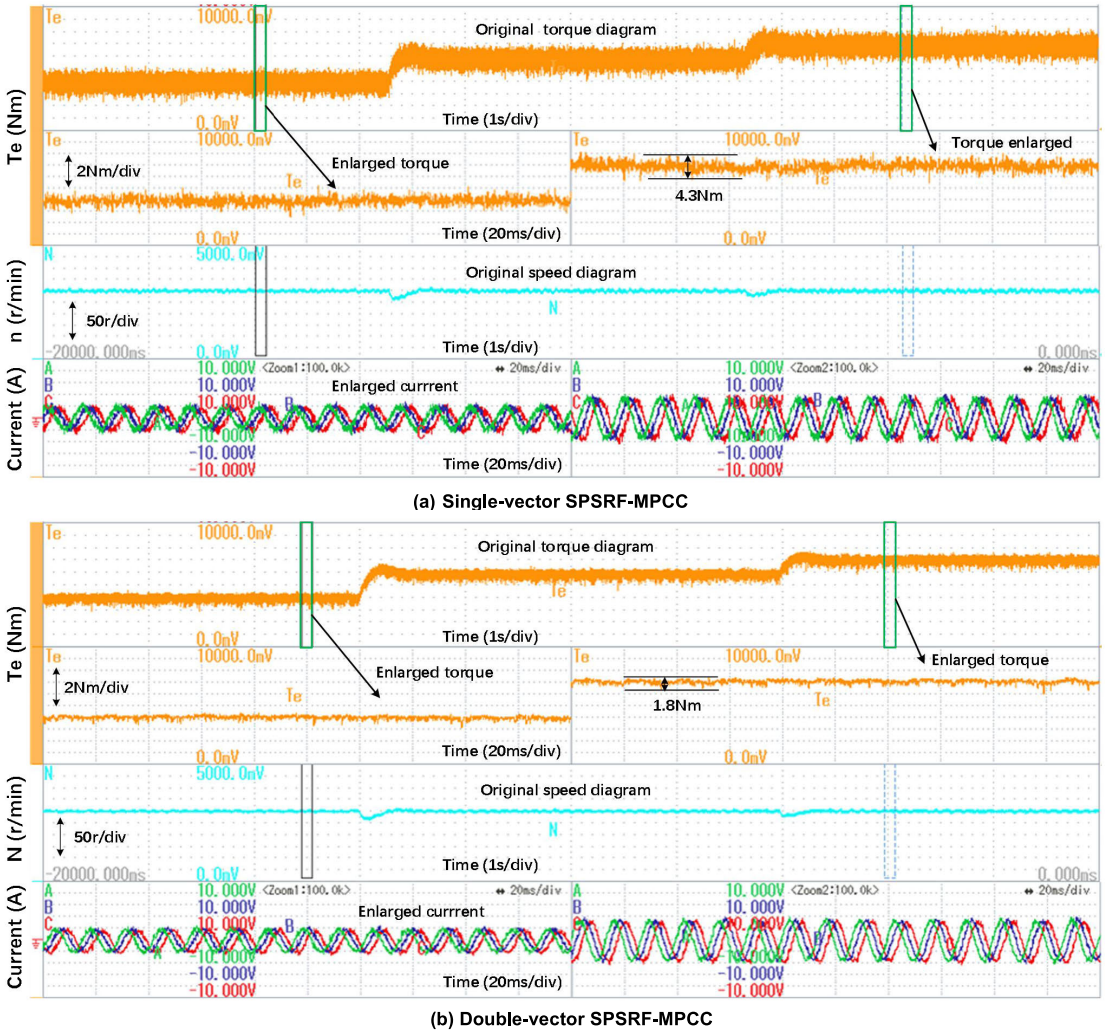

FIGURE 18. Dynamic experimental results of FTPM-RDM using two SPSRF-MPCC algorithms.

the calculation time by eliminating the voltage vector optimization process is significantly improved compared with double-vector RRF-MPCC.

B. VERIFICATION EXPERIMENT OF STEADY-STATE OPERATION

1) EXPERIMENT RESULTS UNDER HEALTHY CONDITION

The first dynamic experiment mainly compares and analyzes the FTPM-RDM in dynamic changes of speed using the single-vector SPSRF-MPCC algorithm and double-vector SPSRF-MPCC algorithm under healthy condition. The FTPM-RDM driving constant 12Nm load and the speed changes by 200r/min-300r/min-400r/min step. Fig.17 shows the torque, speed and current changes when the two methods are adopted. By comparing (a) and (b) in Fig. 17, it is obvious that the current and torque obtained by double-vector SPSRF-MPCC are more accurate than those obtained by single-vector SPSRF-MPCC, and the current distortion and torque ripple are small.

The experiment results show that the improved method can reduce the torque ripple of FTPM-RDM largely, and its control effect of lower speed is more obvious than higher speed situation.

Fig. 18 shows the comparative experimental results of the FTPM-RDM in dynamic changes of load using the single-vector SPSRF-MPCC algorithm and double-vector SPSRF-MPCC algorithm under healthy condition, which mainly include the changes of torque, speed and current. The given speed is stable at 300r/min and the load changes by 8Nm-12Nm-14Nm step. By comparing (a) and (b) in Fig. 18, it is obvious that the current and torque obtained by double-vector SPSRF-MPCC algorithm are more accurate than those obtained by single-vector SPSRF-MPCC algorithm, and the current distortion and torque ripple are small.

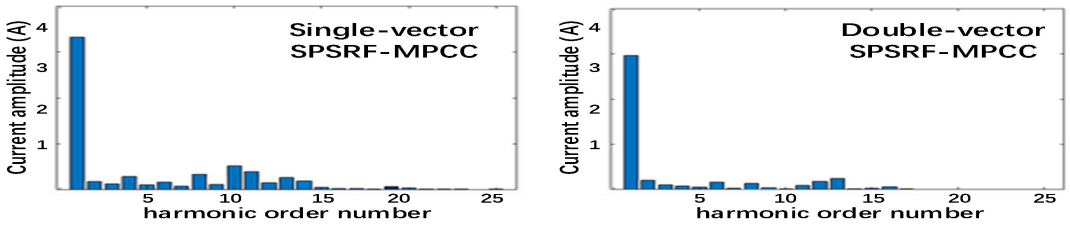

FIGURE 19. Phase A current Fast Fourier Transformation (FFT) diagram of two control algorithms.

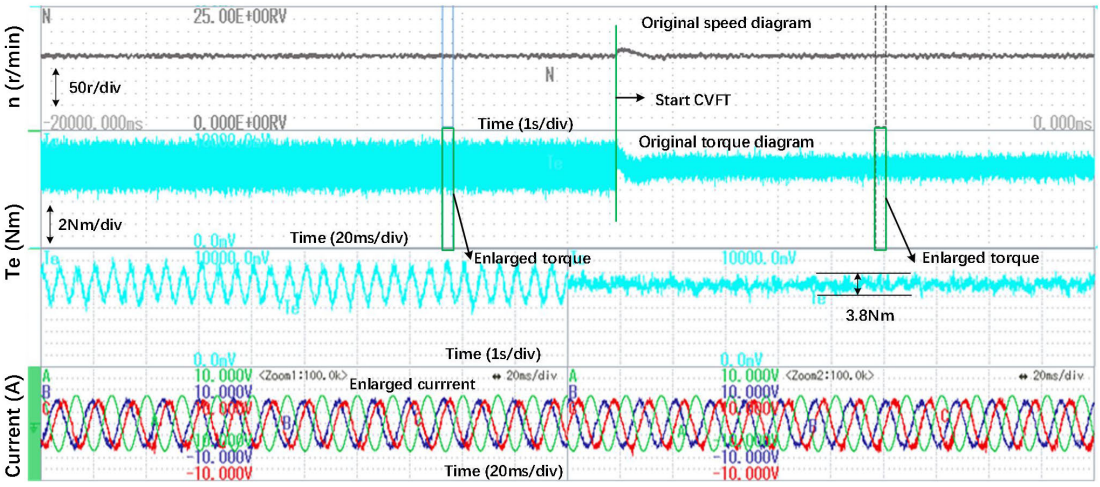

FIGURE 20. Phase a current Fast Fourier Transformation (FFT) diagram of two control algorithms.

The harmonic analysis of six-phase currents is realized by exporting experimental data. Fig. 19 shows the harmonic analysis diagram of current A under the control of the two algorithms. Through comparative calculation, the total distortion of the double-vector SPSRF-MPCC algorithm is reduced from 11.45% to 5.38% compared with the single-vector SPSRF-MPCC algorithm. Combines the current diagram in (a) and (b), the sin property of stator current has been greatly improved.

2) EXPERIMENT RESULTS UNDER ONE-PHASE SHORT-CIRCUIT CONDITION

The motor runs stably at 300r/min with 14Nm load and adopts the double-vector SPSRF-MPCC algorithm to simulate the phase-A short-circuit at a certain time. After the short-circuit runs for a period of time, the fault-tolerant control strategy is added. The experimental results of the process from fault to fault tolerant are shown in Fig. 20 From the diagram, the speed before and after fault-tolerant control is stable. The torque ripple in fault condition is about 26.83%. After adding the fault-tolerant strategy, the torque ripple drops to about 12.21%, which is similar to the simulation situation. Although it is higher than the torque ripple in the stable operation under normal conditions, it ensures the normal and stable operation and is within the acceptable range.

VIII. CONCLUSION

In this paper, a new type of shaftless rim propeller is proposed to be applied to the FTPM-RDM, which can fully improve the ship space utilization and propulsion efficiency while realizing fault-tolerant control under fault conditions. In order to give full play to the efficient application of the MPCC algorithm in the FTPM-RDM, that is, the fast dynamic response and the simple control. Two novel MPCC algorithms based on SPSRF without coordinate transformation are proposed in this paper to reduce torque ripple and computation burden. Both methods can achieve the most effective control by using of the simplest computational steps. First proposed the method of single-vector MPCC algorithm in six phase RRF which groups alternative voltage vectors according to the magnitude of load torque. Although only one vector is selected in each cycle, this method obviously saves computational burden and achieves the control effect of double-vector RRF-MPCC algorithm, indicating that it is feasible and can be further studied in detail. The second method is an improved double-vector combination optimal MPCC algorithm which makes two independent rounds of current prediction for each stator winding and goes through 61 space voltage vectors only 30 times. Compared with double-vector RRF-MPCC, the improved algorithm not only saves operation time without several coordinate transformations, but also significantly improves torque ripple and

control effects. In addition, the fault-tolerant control which is independent of the improved MPCC algorithm proposed in this paper is carried out with the CVFT control strategy under one-phase short-circuit. It is not only does not need to change the control strategy after failure, but also able to suppress the torque ripple effectively. Finally, the simulation and experiment validate the validity and reliability of the two MPCC algorithms under static, dynamic and one-phase short-circuit fault condition. Through comparison, it is found that the double-vector MPCC algorithm can reduce the torque ripple better, and the current harmonics and calculation burden are also decreased significantly. When one-phase short-circuit fault occurs, the torque ripple is also improved by adopting the CVFT method compared with the failure time.

REFERENCES

[1] J. Liu, Z. Gu, and S. Liu, "Research on MDO of ship propulsion shafting dynamics considering the coupling effect of a propeller-shafting-hull system," *Polish Maritime Res.*, vol. 30, no. 1, pp. 86–97, Mar. 2023.

[2] Z. Wang, H. Xiao, and B. Sui, "Review of preventive method for vessel integrated power system," *Ship Electron. Eng.*, vol. 39, no. 11, pp. 159–166, 2019.

[3] W. Li, C. H. Hao, J, Gao, Z. Zou, and J. Pan, "Overview of the development of shipboard integrated power system," *Chin. J. Ship Res.*, vol. 15, vol. 6, pp. 1–11, 2020.

[4] D. W. Brown, J. R. Repp, and O. S. Taylor, "Submersible outboard electric motor/propulsor," *Nav. Eng. J.*, vol. 101, no. 5, pp. 44–52, Sep. 1989.

[5] X. Yan, X. Liang, W. Ouyang, Z. Liu, B. Liu, and J. Lan, "A review of progress and applications of ship shaft-less rim-driven thrusters," *Ocean Eng.*, vol. 144, pp. 142–156, Nov. 2017.

[6] P. Ojaghlu and A. Vahedi, "Specification and design of ring winding axial flux motor for rim-driven thruster of ship electric propulsion," *IEEE Trans. Veh. Technol.*, vol. 68, no. 2, pp. 1318–1326, Feb. 2019.

[7] H. Bai, B. Yu, W. Ouyang, X. Yan, and J. Zhu, "HF-based sensorless control of a FTPMM in ship shaftless rim-driven thruster system," *IEEE Trans. Intell. Transp. Syst.*, vol. 23, no. 9, pp. 16867–16877, Sep. 2022.

[8] D.-K. Hong, D.-S. Joo, J.-Y. Lee, and B.-C. Woo, "Effects of the pole-slot combination on the PMSM of an integrated motor propulsor for an unmanned underwater vehicle considering its electric performance, noise and vibration," *Int. J. Appl. Electromagn. Mech.*, vol. 52, nos. 3–4, pp. 1689–1695, Dec. 2016.

[9] D. Ting, L. Fenghui, and S. Li, "Fault-tolerant method for six-phase PMSM by adjusting phase angle," in *Proc. 20th Int. Conf. Electr. Mach. Syst. (ICEMS)*, Sydney, NSW, Australia, Aug. 2017, pp. 1–5.

[10] R. Ma, J. Zhu, Q. Lin, and Y. Zhang, "Influence of winding distribution on fault tolerant performance in a fault-tolerant permanent magnet rim driven motor," *IEEE Access*, vol. 7, pp. 183236–183244, 2019.

[11] X. Jiang, Z. Zhang, Y. Cai, H. Liu, and K. Wang, "Design and analysis of three-phase FTPMM for partial energy electric pump system," *Energy Rep.*, vol. 9, pp. 671–679, Oct. 2023.

[12] Z. Zhang, Z. Wang, X. Wei, Z. Liang, R. Kennel, and J. Rodriguez, "Space-vector-optimized predictive control for dual three-phase PMSM with quick current response," *IEEE Trans. Power Electron.*, vol. 37, no. 4, pp. 4453–4462, Apr. 2022.

[13] W. Huang, W. Hua, and Q. Fan, "Performance analysis and comparison of two fault-tolerant model predictive control methods for five-phase PMSM drives," *CES Trans. Electr. Mach. Syst.*, vol. 5, no. 4, pp. 311–320, Dec. 2021.

[14] T. Tao, W. Zhao, Y. He, J. Zhu, H. Tan, and R. Xue, "Multivector predictive current control for five-phase PM motor by using hybrid duty modulation technology," *IEEE Trans. Transport. Electrific.*, vol. 6, no. 4, pp. 1603–1612, Dec. 2020.

[15] X. Sun, T. Li, Z. Zhu, G. Lei, Y. Guo, and J. Zhu, "Speed sensorless model predictive current control based on finite position set for PMSHM drives," *IEEE Trans. Transport. Electrific.*, vol. 7, no. 4, pp. 2743–2752, Dec. 2021.

[16] X. Sun, T. Li, M. Yao, G. Lei, Y. Guo, and J. Zhu, "Improved finite-control-set model predictive control with virtual vectors for PMSHM drives," *IEEE Trans. Energy Convers.*, vol. 37, no. 3, pp. 1885–1894, Sep. 2022.

[17] S. G. Petkar and V. K. Thippiripati, "Effective multivector-operated predictive current control of PMSM drive with reduced torque and flux ripple," *IEEE Trans. Transport. Electrific.*, vol. 9, no. 2, pp. 2217–2227, Jun. 2023.

[18] Y. Zhang and H. Yang, "Generalized two-vector-based model-predictive torque control of induction motor drives," *IEEE Trans. Power Electron.*, vol. 30, no. 7, pp. 3818–3829, Jul. 2015.

[19] Y. Xu, B. Zhang, and Q. Zhou, "Two-vector based model predictive current control for permanent magnet synchronous motor," *Trans. China Electrotech. Soc.*, vol. 32, no. 20, pp. 222–230, 2017.

[20] Y. Xu, C. Huang, and J. Wang, "A two-vector-based model predictive current control with online parameter identification for PMSM drives," *Proc. CSEE*, vol. 12, no. 30, pp. 1–13, 2022.

[21] H. Wang, X. Zheng, X. Yuan, and X. Wu, "Enhanced natural fault-tolerant model predictive current control in nine-phase motor drives under open-phase faults," *IEEE Trans. Energy Convers.*, vol. 37, no. 4, pp. 2449–2460, Dec. 2022.

[22] X. Sun, T. Li, X. Tian, and J. Zhu, "Fault-tolerant operation of a six-phase permanent magnet synchronous hub motor based on model predictive current control with virtual voltage vectors," *IEEE Trans. Energy Convers.*, vol. 37, no. 1, pp. 337–346, Mar. 2022.

[23] N. Simpson, D. J. North, S. M. Collins, and P. H. Mellor, "Additive manufacturing of shaped profile windings for minimal AC loss in electrical machines," *IEEE Trans. Ind. Appl.*, vol. 56, no. 3, pp. 2510–2519, May 2020.

[24] W. Huang, X. Zhu, H. Zhang, and W. Hua, "Generalized fault-tolerant model predictive control of five-phase PMSM drives under single/two open-switch faults," *IEEE Trans. Ind. Electron.*, vol. 70, no. 8, pp. 7569–7579, Aug. 2023.

[25] Y. Ji, H. Zhao, and J. Zhu, "Direct torque control strategy of permanent magnet fault-tolerant rim driven motor under open circuit fault," *J. Dalian Maritime Univ.*, vol. 45, no. 4, pp. 110–116, 2019.

[26] H. Bai and B. Yu, "Position estimation of fault-tolerant permanent magnet motor in electric power propulsion ship system," *IEEJ Trans. Electr. Electron. Eng.*, vol. 17, no. 6, pp. 890–898, Jun. 2022.

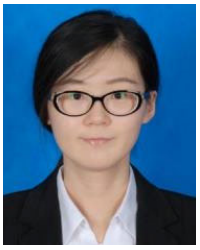

YONGHAN LIU (Student Member, IEEE) received the B.Eng. degree in electrical engineering and automation from Binzhou University, Binzhou, China, in 2013, and the M.S. degree in control science and engineering from Dalian Maritime University, Dalian, China, in 2017, where she is currently pursuing the Ph.D. degree in marine electrical engineering. Her research interest includes position sensorless control of FTPMM.

JINGWEI ZHU (Member, IEEE) received the B.Eng. degree in automation instrumentation from the Jinzhou Institute of Technology, Jinzhou, China, in 1985, the M.S. degree in electronic engineering from the Shenyang University of Technology, Shenyang, China, in 1990, and the Ph.D. degree in electrical engineering from The Adelaide University, Adelaide, Australia, in 2008. He was a Lecturer and an Associate Professor with the Jinzhou Institute of Technology, from 1985 to 1999. In 2000, he joined the Marine Electrical Engineering College, Dalian Maritime University, China, where he is currently a Professor. His research interests include designs and control for electrical machine systems, power electronic devices, and sustainable energy generation.

JIUBO YUE received the bachelor's degree in electrical engineering and automation from Dalian Maritime University, Dalian, China, in 2020, where he is currently pursuing the master's degree in power electronics and electric drive. His research interest includes motor control.

JIANG WU received the bachelor's degree in electrical engineering and automation from Liaoning Shihua University, in 2015, and the master's degree in control science and engineering from Dalian Maritime University, in 2019, where he is currently pursuing the Ph.D. degree in ship electrical engineering. His research interests include advanced motor control algorithm and motor fault diagnosis.

PING REN (Student Member, IEEE) received the B.S. degree in electrical engineering and automation from Liaoning Shihua University, Fushun, China, in 2016, and the M.S. degree in electronic engineering from Dalian Maritime University, Dalian, China, in 2019, where she is currently pursuing the Ph.D. degree in marine electrical engineering. Her research interests include design, analysis, and control of high-performance switched reluctance motors.

XIANG LI received the B.Eng. and M.S. degrees in traffic and transportation engineering from Dalian Maritime University, Dalian, China, in 2020 and 2023, respectively. His research interest includes control of FTPMM.